31st Symposium on Naval Hydrodynamics
Monterey, California, 11-16 September 2016

An acoustic analogy and scale-resolving flow simulation methodology for the prediction of propeller radiated noise

R.E. Bensow[1] and M. Liefvendahl[1,2]
([1]Chalmers University of Technology, Sweden, [2]Swedish Defence Research Agency, FOI)

ABSTRACT

A methodology for the prediction of underwater radiated noise from ships is presented and applied to a configuration of a cavitating propeller, operating in behind condition. A scale resolved incompressible Large Eddy Simulation technique together with an acoustic analogy is employed, with cavitation represented through a mixture assumption using a volume of fluid approach and explicit mass transfer modelling. The main configuration studied is the catamaran hull and propeller of a small research vessel in model scale. The hull and a complete geometrical model of the propeller is included, while the free surface is neglected in the simulation. Results of radiated noise from the complete configuration are presented and compared with experimental data. Further, as an intermediate step, the propeller alone on inclined shaft is studied for both cavitating and non-cavitating conditions.

INTRODUCTION

Prediction of cavitation noise from vessels during the design phase is a challenging task, both when using model tests and numerical predictions. For an assessment over a broad frequency range, the model tests need to be performed in a large and silent environment. Simulation methodologies suffer from high resolution requirements, modelling issues related to cavitation, as well as techniques to propagate the noise to a far field (relatively speaking) virtual hydrophone. The issue of cavitation noise prediction is primarily relevant for commercial vessels, in anticipation of increasing regulations on shipping noise, while, for instance submarines normally operate without cavitation; however, prediction of noise signature from non-cavitating conditions partly suffers from the same difficulties. Never the less, it is expected that an increased attention on shipping noise as an environmental concern will lead to regulations on underwater radiated noise levels on new designs.

Considerable effort has been spent in the recently ended European research projects AQUO and SONIC, within the European Union 7th Framework Programme, to improve both experimental and numerical prediction of cavitation noise. Within the SONIC project[1], the research vessel of the University of Newcastle, the R/V Princess Royal, was investigated by several partners, in different test facilities and with different numerical prediction methodologies, as well as with measurements of noise from the full scale vessel. Within the project, Chalmers implemented, verified, and validated a propagation modelling methodology based on the Ffowcs-Williams and Hawkings approach (Ffowcs-Williams and Hawkings, 1969), where the noise sources are encapsulated within an integration surface and then propagated to a far field observer; we refer to this approach as an acoustic analogy. This paper will present our efforts to analyse the flow around the R/V Princess Royal using LES, Large Eddy Simulation, techniques and the acoustic analogy and perform predictions of radiated noise.

The use of scale-resolving CFD together with acoustic analogies is in a pioneering state for marine and naval applications. Although the simulation technique is expensive, in terms of the need for highly resolved simulations and long time series, the potential to perform noise prediction is expected to be high, with the prospect of yielding improved understanding of noise generating flow mechanisms, both in general terms and in specific design studies. This can be expected to be enhanced by complementing experimental and computational techniques. The knowledge developed will become useful in the design of more silent vessels, without compromising the propulsive efficiency.

The costly simulations are deemed necessary, as shown in this paper as well as our previous studying on transient flow features affecting the propulsion system (Bensow, 2015, Liefvendahl and Bensow, 2014). The wake behind a commercial vessel is dominated by a complex and highly unsteady flow forming the inflow to the propeller. Both blade loading and cavitation dynamics are affected by this, and will have a large impact on the radiated noise.

However, we emphasise that there are several unre-

[1]SONIC, grant agreement 314394, European Union 7th Framework Programme

solved issues with the methodology. The usage of acoustic analogies is largely untested in the relevant parameter range for ship noise applications, where the Mach (Ma) number normally is well below 0.1. In a cavitating flow, as is normal conditions for a modern merchant vessel, volume noise sources are expected to dominate the surface sources. These are normally modelled in the simulation by a mixture assumption. It is not yet established how well the sampling of flow variables on an integration surface represents the actual noise source, nor how this integration surface should be located. Further, the lack of good and simple validation material for this kind of flow hinders the evaluation, as is noted in this paper.

The objective of this paper is to present early experiences in using this methodology in predicting propeller radiated noise. This concerns both the potential gain in understanding flow mechanisms influencing noise generation, as well as the practical issues in developing and applying the methodology in realistic ship applications.

The structure of the paper is as follows. First, an overview of the simulation methodology is given, presenting the flow modelling, how cavitation is handled, and the basis of the acoustic analogy. We then proceed to present validation of the methodology for a low-Ma aeroacoustic application, based on recently published wind tunnel tests on sound from cylinders. For the ship noise prediction of the R/V Princess Royal, the study was split in two: the propeller alone on an inclined shaft, simulated both in cavitating and non-cavitating conditions, then the hull and propeller together. For all three application examples, features of the flow field is first presented, then acoustic results are analysed.

METHODS

A summary of the flow and acoustic models, as well as the numerical methods employed, is given in this section. A two-stage process, based on a so-called acoustic analogy, is used, as described below. The flow of the noise generating mechanisms is first simulated, and then the resulting noise sources are computed from the simulated flow. Thus there is a one-way coupling from the flow to the noise generation. The integral representation of the acoustic pressure, proposed by Francescantonio (1997), is used for the radiated sound.

Flow modelling

In the absence of cavitation, the flow is modelled by the incompressible Navier-Stokes equations. Low-pass filtering of the equations, and neglecting commutation errors (Sagaut, 2002), the fundamental LES-equations for incompressible flow are obtained,

$$\frac{\partial \mathbf{v}}{\partial t} + \nabla(\mathbf{v} \otimes \mathbf{v}) = -\frac{1}{\rho_0}\nabla p + \nabla \cdot (\mathbf{S} - \mathbf{B}) \qquad (1)$$

Here, $\mathbf{v}$ is the (filtered) velocity field, ρ_0 is the density, p is the pressure, $\mathbf{S} = 2\nu\mathbf{D}$ the viscous strain tensor, $\mathbf{D} = (\nabla\mathbf{v} + \nabla\mathbf{v}^T)/2$ the rate-of-strain tensor, and ν the kinematic viscosity. The term in equation (1) which arises from the filtering is the subgrid stress tensor $\mathbf{B}$. No special notation is used to distinguish between the primary and filtered variables, i.e. $\mathbf{v}$ is used for both filtered and unfiltered velocity. Below we will introduce notation with primed variables (e.g. p') for acoustic quantities. This notation convention is used throughout all sections of the paper. It is referred to Sagaut (2002) as a general reference for LES, and to Fureby (2008), and the references therein, for LES applied to problems in naval hydrodynamics.

The subgrid modelling away from walls, consists of the expression for the subgrid stress tensor. In this paper, we only present results using an implicit LES modelling approach, where the subgrid dissipation is considered to be represented by numerical diffusion, see e.g. Grinstein et al. (2007). This approach has previously been used successfully, see, e.g., Fureby (2008) for several applications in wetted flows and Bensow and Bark (2010) for cavitating flows. Further, in the cylinder simulations, we have utilised a mixed formulation, following Bensow and Fureby (2007), where the scale similarity term is considered a resolved part of the filtered momentum equations.

The flow in a turbulent boundary layer at the wall requires special subgrid modelling, see Piomelli (2008) for a review. Here a simple model is used which relies on the law-of-the wall by Spalding (1961), to modify the subgrid viscosity at the wall, ν_{nw}, according to,

$$\nu_{nw} + \nu = u_\tau^2 \Bigg/ \left|\frac{\partial v_\parallel}{\partial y_\perp}\right|_p ,$$

where $u_\tau = \sqrt{\tau_w/\rho_0}$, is the friction velocity, τ_w the wall-shear stress, $v_\parallel$ the flow velocity component parallel to the wall, $y_\perp$ the local coordinate perpendicular to the wall, and the sub-script p indicates evaluation in the first cell center next to the wall.

Multiphase modelling

To simulate cavitating flows, the two phases, liquid and vapour, need to be represented in the problem, as well as the phase transition mechanism between the two. Here, we consider a one fluid, two-phase mixture approach, introduced through the local vapour volume fraction, α_v, and having the spatial and temporal variation of the vapour fraction described by a scalar transport equation including source terms for the mass transfer rate between

the phases, $\dot{m}$. The density ρ_0 and dynamic viscosity μ are assumed to vary linearly with the vapour fraction in the mixture,

$$\rho_0 = \alpha\rho_v + (1-\alpha)\rho_l, \quad \mu = \alpha\mu_v + (1-\alpha)\mu_l,$$

with the bulk values, ρ_v, ρ_l, μ_v, and μ_l, kept constant. Using this expression for the density in the continuity equation, it is straight forward to derive the non-homogeneous velocity divergence due to the mass transfer between the phases,

$$\nabla \cdot \mathbf{v} = \left(\tfrac{1}{\rho_v} - \tfrac{1}{\rho_l}\right)\dot{m}, \tag{2}$$

that implies that the pressure correction equation in the segregated solver algorithm needs to be modified as well.

In the current study, the mass transfer model proposed by Sauer (2000) is employed,

$$\dot{m} = \mathrm{sign}(p - p_{\mathrm{th}})\frac{\alpha_{\mathrm{l}}(1-\alpha_{\mathrm{l}})}{R_{\mathrm{B}}}\frac{3\rho_{\mathrm{l}}\rho_{\mathrm{v}}}{\rho_{\mathrm{m}}}\sqrt{\frac{2\,|p-p_{\mathrm{th}}|}{3\rho_{\mathrm{l}}}}, \tag{3}$$

where average nucleus per liquid volume is considered constant and in this study set to $n_0 = 10^8$, and the initial nuclei radius is $d_{Nuc} = 10^{-4}$ m. Further, the modifications proposed by Asnaghi (2015) have been used, where the vaporisation component of Equation 3 is multiplied by a variable C_v based on local flow time scales,

$$C_{\mathrm{v}} = (1 + t_\infty\,|\mathbf{D}|)\,,$$

and the local shear stress is considered in the pressure threshold,

$$p_{\mathrm{threshold}} = \mu\dot{\gamma} + p_{\mathrm{Sat}}, \quad \mu\dot{\gamma} = \sqrt{\mathbf{D}:\mathbf{D}}.$$

The acoustic analogy

The method used here for prediction of radiated noise is derived from the class of acoustic analogies described in the landmark paper by Ffowcs-Williams and Hawkings (1969). The general situation of interest consists of sound generated by unsteady flow in a certain region, and then radiated out from this region. An acoustic analogy consists of an exact reformulation of the governing fluid flow equations, to obtain an equation with a left-hand side consisting of the wave operator (d'Alembertian), operating on the acoustic pressure (or density), and a right-hand side with the remaining terms, representing the sources of flow-generated noise.

The free-space (acoustic) Green's function can then be used to solve this wave equation, leading to an integral representation for the acoustic field. A number of different such integral representations have been suggested in the literature. The version suggested by Francescantonio (1997) is used here. It consists of integration over a porous surface S which is chosen judiciously with respect to the flow. In the low Mach-number range, the expression for the acoustic pressure p' takes the following form,

$$4\pi p'(\mathbf{x},t) = I_1 + I_2 + I_3 + p'_Q, \tag{4}$$

where, p'_Q is the acoustic pressure generated by sources outside of S, and the three surface integrals are given by:

$$\begin{aligned} I_1 &= \frac{\partial}{\partial t}\int_S \left[\frac{\rho_0 U_n}{r}\right]_\tau \mathrm{d}S_{\mathbf{y}}, \\ I_2 &= \frac{1}{c_0}\frac{\partial}{\partial t}\int_S \left[\frac{L_r}{r}\right]_\tau \mathrm{d}S_{\mathbf{y}}, \\ I_3 &= \int_S \left[\frac{L_r}{r^2}\right]_\tau \mathrm{d}S_{\mathbf{y}}. \end{aligned}$$

Here, the coordinate $\mathbf{y}$ denotes the source (integration) point, $\mathbf{x}$ denotes the acoustic field point, $r = |\mathbf{x}-\mathbf{y}|$ is the distance between these points, $\tau = t - r/c_0$, is the retarded time and c_0 is the speed of sound. The notation for the remaining two quantities in the integrals is explained next. First we introduce $\mathbf{u}$ for the local velocity of the surface S, $\mathbf{e}_n$ for the outward pointing unit normal to the surface S, and $\mathbf{e}_r = (\mathbf{x}-\mathbf{y})/r$ for the unit vector in the direction from source point to field point. For any vector $\mathbf{f}$, the components along these two directions are then denoted, $f_n = \mathbf{f}\cdot\mathbf{e}_n$, and $f_r = \mathbf{f}\cdot\mathbf{e}_r$ respectively. Now, U_n is the normal component of the vector,

$$\mathbf{U} = \left(1 - \frac{\rho}{\rho_0}\right)\mathbf{u} + \frac{\rho}{\rho_0}\mathbf{v},$$

and L_r is the r-component of the vector,

$$\mathbf{L} = p\mathbf{e}_n + \rho\mathbf{v}(v_n - u_n).$$

As compared to Francescantonio (1997), the assumption, $1 - \mathrm{Ma} \approx 1$ has been used in the expression for the integral representation. This assumption of low Mach number is good for most naval applications, with the exception of regions with air/vapour/liquid mixture. For instance, usually $\mathrm{Ma} < 0.02$ based on the propeller blade tip speed. The highest Mach number in the reported simulations of this paper is the acoustic wind tunnel measurements of noise from a cylinder in cross flow, for which $\mathrm{Ma} = 0.155$.

A practical, and crucial, aspect of the use of this method is the choice of where to place the integration surface S. It should enclose most noise sources. For most naval applications, where cavitation is not considered, this is relatively easy, since the dominant sources typically are located at material surfaces at low Mach number, (Blake, 1986, Curle, 1955). The usage of acoustic analogies for cavitating flows is an unproven technique where best practices are not established. Only a few attempts have been presented: Li et al. (2015), Lidtke et al. (2015), and Lidtke et al. (2016). Of these, only the first have validation data

while the other two are only feasibility studies. There are several uncertainties in how to use this approach, with respect to the use of a sampling surface, how volume variation induced by cavitation is treated, and of course the compressible collapse of cavitating structures. Best practise guidelines for the surface placement are thus not available, and the practical choice is discussed in connection with the different cases reported in the paper.

Numerical methods

The solvers which are used are implemented using the open source software package OpenFOAM[2], which provides an object-oriented library, based on the finite-volume method, specifically designed for CFD; see Weller et al. (1998) for a description of the structure of this software design.

The discretization of the governing flow equations relies on storage of the unknown flow variables in the cell-center positions in the computational grid. The algorithm supports arbitrary polyhedral cells and the grid is treated as unstructured. The approximations involved are of second-order accuracy, except for flux limiting for the convective term, which reduces locally the formal order of accuracy near sharp gradients. The momentum equation is treated in a segregated manner, solving sequentially the three components of the momentum equations in a loop within each time step. This is done through a merged version of the SIMPLE (Patankar and Spalding, 1972) and PISO algorithms, where the PISO loop is complemented by an outer iteration loop and possible under-relaxation of the variables, called PIMPLE in OpenFOAM; see e.g. Barton (1998) for different ways to merge PISO and SIMPLE procedures. For the cavitating flow simulations, the mass transfer sources are computed first in the PISO loop, then the vapour fraction transport is progressed, and finally the standard PISO procedure is entered.

The simulations are time resolved and a second order backward differencing scheme is used for the time advancement of the components of the momentum equation. A domain decomposition technique, applied to the grid, in combination with an efficient MPI-implementation is used for running on parallel computers.

The inclusion of a moving component (in this case the propeller) is performed using the sliding-interface implementation in OpenFOAM. Interpolation is performed between the non-conforming interfaces between two regions, based on the interpolation algorithm by Farrell and Maddison (2011), denoted as AMI (Arbitrary Mesh Interface). This constitutes an efficient and conservative interpolation between non-conforming mesh interfaces based on Galerkin projection. The AMI has been shown to show good performance regarding both scalability and conservation of the flow quantities (Bensow, 2013, Turunen, 2014). Further, the AMI has also been used to coarsen the mesh towards the outer domain in the cylinder simulations by introducing hanging nodes, see further below.

The acoustic computation, using equation (4), is carried out as a post-processing step relative to the flow simulation. During the flow simulation, the quantities involved in the acoustic surface integrals are saved to file. This requires special pre-processing for the flow simulation, in which the acoustic surface is set up as a set of faces of the finite volume cells in the flow computation grid. This face set is then used in the discretization of the acoustic integrals. Additional input to the acoustic computation is a set of acoutic field points, referred to as micro- or hydrophones below (depending on whether the sound occurs in air or water). This implies that only one flow simulation is necessary for the processing of any number of field points. If the acoustic surface is modified however, then it is necessary to re-run the flow simulation.

VALIDATION FOR A CYLINDER IN CROSS FLOW

A cylinder in cross flow is a canonical flow problem which has been extensively investigated using both experimental methods, see e.g. Cantwell and Coles (1983), and simulations, see e.g. Franke and Frank (2002), Parnaudeau et al. (2008). The vortex shedding at the cylinder is a significant sound source, and a number of studies have been dedicated to this aspect. Measurements were reported by Etkin et al. (1957), and the sound generation was investigated by simulations by Cox et al. (1998) and Pérot et al. (2003). A range of Reynolds and Mach numbers were investigated in the cited studies.

In this section, we carry out a validation study using the very recent and well documented sound measurements, carried out in an aero-acoustic wind tunnel, reported by LaTorre-Iglesias et al. (2016). One case was simulated, with physical parameters given in Table 1.

In the experiments, the cylinder is placed in an open jet, and a length of $L_e = 22D$, of the cylinder, is located in the clean flow. The main sound generation mechanism is the pressure fluctuations on the cylinder surface, caused by the periodic vortex shedding. The shedding frequency is approximately $f_s = 830\,\text{Hz}$, based on an approximate Strouhal (St-)number $\text{St} = Df_s/V_0 = 0.2$, see below for the actual calculated St-number. This shedding frequency corresponds to an acoustic wave length of $\lambda_s = 0.41\,\text{m}$. Comparing this to the cylinder length scales, we obtain $D/\lambda_s \approx 0.03$, $L/\lambda_s \approx 0.14$ and, $L_e/\lambda_s \approx 0.64$. Hence it is reasonable to consider the cylinder to be an acoustically compact source. The radiated sound will be computed at

[2] www.openfoam.com

a distance of $5\,\mathrm{m} \approx 12\lambda_s$, from the cylinder, which can be considered to be in the acoustic far field.

Both a cartesian (x,y,z) and a cylindrical (r,θ,y) coordinate system are used. The y-axis is coincident in the two systems, and located on the cylinder axis, with the cylinder occupying the region, $0 < y < L$. The x-axis of the cartesian system is directed in the main flow direction, with $x = 0$ on the cylinder axis, and the z-axis is taken to form a right-handed system. The cylindrical angle, $\theta = 0$, is located at the stagnation point/line of the flow around the cylinder.

The standard deviation of the acoustic pressure $\sigma(p')$, in the far field can, for the acoustically compact case, be approximately expressed as,

$$\sigma(p')^2 = \frac{\rho_0^2 V_0^6 \mathrm{St}^2 \sigma(C_l)^2 L l_c D}{16 c_0^2 r^2} \sin^2\theta. \qquad (5)$$

This expression was first derived by Phillips (1956), see also chapter 4 of Blake (1986) for a comprehensive treatment using the methods available at the time (i.e. no computational acoustics). In Equation (5), ρ_0 denotes the density, C_l the lift coefficient, $\sigma(\cdot)$ the standard deviation, and l_c the axial correlation length of the (transversal) fluid force on the cylinder non-dimensionalized with D. The lift coefficent is defined by,

$$C_l(t) = \frac{F_z(t)}{DL\rho_0 V_0^2/2},$$

where F_z is the z-component of the total force on the cylinder. The drag coefficient is defined by the corresponding expression involving F_x instead, and is denoted C_d. Results will be presented for both the mean $m(\cdot)$ and the standard deviation $\sigma(\cdot)$ of the force coefficents and other quantities. The mean and the standard deviation are computed from the simulated time series, after the initial transient.

Table 1: Physical parameters for the simulated cylinder case. The Re-number is based on the cylinder diameter, $\mathrm{Re} = V_0 D/\nu$.

Quantity	Notation	Value	Unit
Cylinder diameter	D	0.012	m
Cylinder length	L	0.060	m
Kinematic viscosity	ν	$1.46{\cdot}10^{-5}$	m^2/s
Speed of sound	c_0	345	m/s
Free-stream velocity	V_0	50.0	m/s
Reynolds number	Re	41 100	- - -
Mach number	Ma	0.155	- - -

Pre-processing and numerical parameters

Simulations have been performed based on an implicit LES approach with the scale similarity term included, following Bensow and Fureby (2007), not using any wall model. This is motivated by the low Reynolds number which is expected to yield a laminar boundary layer upstream of the separation point. A TVD limited central differencing convective scheme is used to achieve proper numerical diffusion (Bensow and Liefvendahl, 2008). The time step was defined to give a maximum Courant number of around 0.5, with average over all cells of around 0.01. The simulations were first run to a well developed flow on a slightly coarser computational mesh, then mapped to the final mesh described below and further ran for 200 flow pass times, D/V_0, before averaging and sampling were initiated. Results presented below are then based on 400 flow pass times, corresponding to approximately 80 shedding cycles, based on $St = 0.2$.

The computational domain used has the cylinder located at $(0,0,0)$, expanding in spanwise direction to $(0,0.012,0)$. The inlet is placed $15D$ upstreams, outlet $45D$ downstream, and the vertical extent is $15D$ in each direction. The main flow is in the positive x-direction.

The final mesh is a fully structured hexahedral mesh, but using hanging nodes in a 2:1 mesh ratio in the spanwise direction to save cells towards the outer boundary. The hanging node interface is placed approximately $7D$ from the cylinder in radial direction and extending $25D$ downstream, thus well outside the domain where important flow dynamics is present. The total number of cells is 4.7 M. Spanwise spatial resolution is $\Delta y = 0.05D$, which is deemed sufficient (Parnaudeau et al., 2008). Further, cells are clustered in the laminar boundary layer and in the separated shear layer behind the cylinder with 460 cells in the circumferential direction and approximately 10 cells across the boundary layer.

Table 2: Time advancement parameters. The start time of the simulation on the final grid is denoted T_0, T_1 is the time instant when the transients in the flow are expected to have passed, and T_2 is the end time of the simulation.

$\Delta t(\mu\mathrm{s})$	$T_0(\mathrm{s})$	$T_1(\mathrm{s})$	$T_2(\mathrm{s})$
0.5	0	0.048	0.144

In order to investigate the span wise correlation of the flow, lift and drag forces are separately computed for 10 non-overlapping sections, with span wise extent $0.1L$, across the cylinder. Corresponding "sectional" drag coefficients are then defined by,

$$C_d^{(i)} = \frac{F_x^{(i)}(t)}{DL\rho_0 V_0^2/2},$$

for $i = 1,\ldots,10$. Here $F_x^{(i)}$ is the force acting on cylinder section i. In the analogous manner, sectional lift coefficients $C_l^{(i)}$ are also defined. Furthermore, a special measure of the standard deviation of the forces is introduced,

which is appropriate for the sections of the cylinder:

$$\sigma_s(C_d) = m\left[\sigma\left(C_d^{(i)}\right)\right]$$

For the acoustic analysis, the cylinder surface itself was primarily used for sampling of acoustic sources. In addition to this, two more sampling surfaces were included in the computation: one formed from a circular tube enclosing the cylinder with radius $2.5D$, and one formed from the faces where there are hanging nodes, as described above. The first is thus closed, with flow structures moving through the surface, while the second is open.

During post-processing, microphones are placed at a distance of 5 m in circles around the centre of the cylinder, aligned with the coordinate axes, with $\Delta\theta = 10°$. The analysis is here limited to the microphones in the xz-plane, perpendicular to the cylinder axis at $L/2$. The 36 microphones are numbered starting in the top position, with H_0 at coordinate $(r, y, \theta) = (5\text{m}, 0.03\text{m}, 90^o)$, with numbering increasing behind the cylinder (downstream) with microphone H_9 at coordinate $(r, y, \theta) = (5\text{m}, 0.03\text{m}, 180^o)$, and so forth along the circle in the xz-plane.

Flow results

The flow around an infinite circular cylinder is well known and in general well documented, especially at $Re = 3,900$ and around $Re = 140,000$, but not at the currently studied condition. As a separate validation study, we performed simulations at $Re = 3,900$ using the same computational configuration as presented above. The results, not presented here for brevity, showed good agreement with the experiments and LES presented in Parnaudeau et al. (2008). The predicted flow at the higher $Re = 41,100$, is presented in Figure 2, with integral quantities tabulated in Table 3. The recirculation zone is rather short, as instabilities quickly grow in the shear layer dvelopping after the top and bottom of the cylinder. Further, integral quantities are in the expected range.

For the radiated noise, coherent flow structures depending on the span-wise extension of the cylinder is important. Close to the cylinder surface, there are no notable coherent structures developing cross the cylinder, but moving further down stream, clear longitudinal co-rotating structures are being developed, as expected. These latter have however little impact on noise. To clarify the amount of span-wise correlation, the sectional lift coefficients, as defined above, is plotted in Figure 1 for a short time span. The lift of each section (grey lines) are more or less in sync with the average flow (bold black line) for the whole time period.

Table 3: Results for integral quantities on the cylinder.

St	$m(C_d)$	$\sigma(C_l)$	$\sigma_s(C_l)$	$m(\theta_{sep})$
0.191	1.34	0.67	0.70	88^o

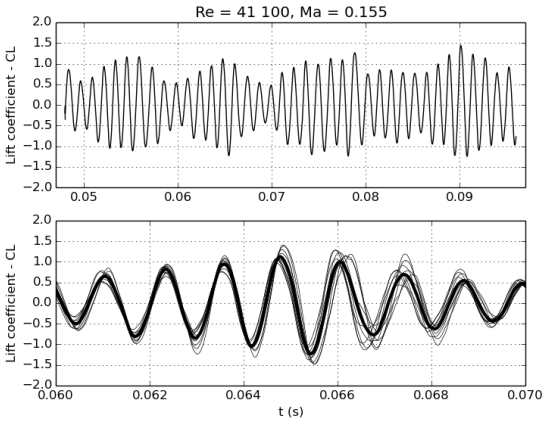

Figure 1: Time history of the lift coefficient. Above: The lift coefficient computed for the whole cylinder, plotted for the complete simulated time interval. Below: The lift coefficients computed for the segments (10 lines)

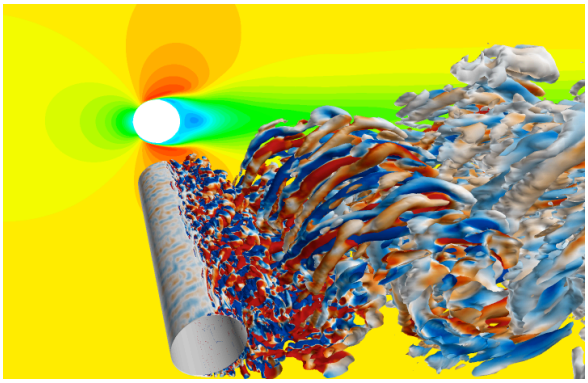

Figure 2: Visualization of computed flow for the circular cylinder; flow structure isosurface coloured by axial vorticity and contours of the mean axial velocity.

Acoustic results

The source levels in 1/3-octave band from the simulation are compared with the measurements of LaTorre-Iglesias et al. (2016) in Figure 3. The amplitude of the microphone signals, both for the simulation and measurement, have been re-scaled (using $p' \sim 1/r$) to obtain source levels relative to a distance of 1 m. The simulation data are taken from microphone H_0. The cylinder length is different between the simulation and the measurements ($5D$ vs $22D$). Therefore, the computed source level shifted, $+6\,\text{dB} \approx 10\log_{10}(22/5)\,\text{dB}$, is also included in Figure 3. This corresponds to the summation of the contribution of uncorrelated sources, which roughly amounts to the assumption, $l_c < 5$, for the spanwise correlation length.

The source levels (dB) corresponding to the results in Figure 3 are given in Table 4. Source levels obtained using the dipole expression (5) are also included for comparison. The main source of uncertainty concerning the

simulation results is believed to be related to the spanwise correlation length l_c. As is clear from the cylinder radation expression (5), this directly affects the amplitude of the radiation. At the same time, the scatter plot of the sectional lift coefficients in Figure 1, clearly indicates a relatively strong correlation over the spanwise extent of the simulation domain. To indicate the sensitivity to correlation length, two estimates of l_c are used in the dipole results given in Table 4.

The directivity of the radiated sound is shown in Figure 4 in the xz-plane. Both the directivity of the simulation results and the experiments are included, as well as the directivity of an ideal dipole aligned with the z-axis. Both the simulation and experimental data are dominated by a dipole pattern. For the experiments, there is a skew, with slightly stronger radiation in the upstream direction, compare the angle $\theta \approx 60^o$, and the angle, $\theta \approx 120^o$.

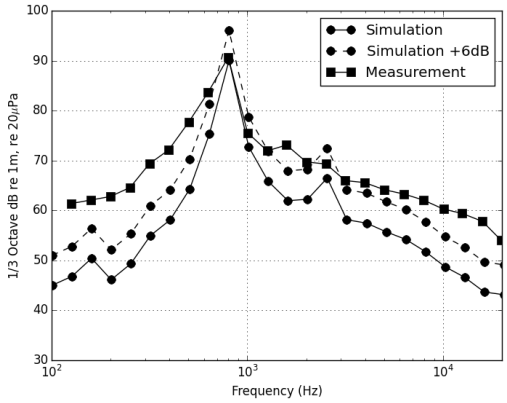

Figure 3: Comparison of the source 1/3-octave band level with the measurements of LaTorre-Iglesias et al. (2016). Data from microphones in the main (dipole) radiation direction, $\theta = \pm 90^o$.

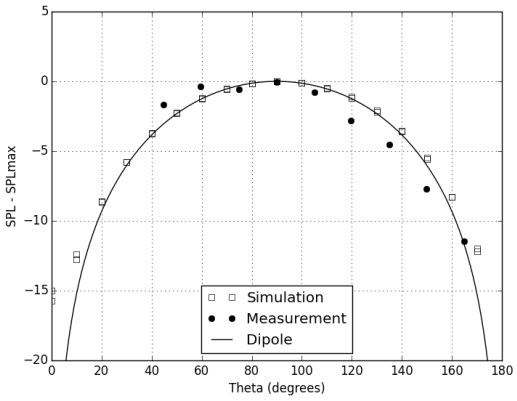

Figure 4: Directivity of the acoustic radiation from the cylinder, shown in terms of the source level relative its maximum value (for $\theta \approx 90^o$). Data from the simulation, from the experiments LaTorre-Iglesias et al. (2016), and for an ideal dipole aligned with the z-axis.

Table 4: Source level (dB re 1 m, 20μPa) in the main (dipole) radiation direction, $\theta = \pm 90^o$. The last two columns give results obtained using the dipole radiation, equation (5), with different assumption concerning the correlation length l_c. The minimum value being obtained with $l_c = 5$, and the maximum with $l_c = 22$. The remaining parameters in the dipole expression are determined from the simulation.

Sim.	Sim. +6dB	Exp.	min.dip.	max.dip.
90.3	96.4	92.0	91.2	97.6

THE RESEARCH VESSEL PRINCESS ROYAL

The R/V Princess Royal is a research vessel designed and operated by the University of Newcastle (Atlar et al., 2013), to support the marine research activities of the university. The design was based on the catamaran application of the displacement type Deep-V hull forms with a novel anti-slamming bulbous bow and tunnel stern accommodating the propeller and rudder; propeller tip-hull clearance is reported to be 15% of the propeller diameter and the clearance to the skeg plating, extending aft to support the rudder mounting, is 10%. The vessel was fitted with two five bladed fixed pitch propellers, one on each hull, operating in an outward turning rotation; we have simulated the configuration as of the tests in 2015.

It is a small, versatile and relatively high speed vessel, that can be equipped for different research studies. It was used for studies on inboard and underwater radiated noise within the EU-project SONIC[3]. The vessel was tested at several facilities in model scale during the SONIC project, and noise measurements were performed for the full scale vessel in two separate campaigns, encompassing both inboard noise and vibration measurements, cavitation observations, and radiated noise from hydrophone measurements in the North Sea. As a partner in the SONIC project, we have thus chosen to continue the studies for this well documented case (Aktas et al., 2015, 2016, SONIC, 2015a,b); see also Felli et al. (2015) on the experimental techniques used to perform the noise measurements used below. The main dimensions for the model as tested at CNR-INSEAN with the scale factor $\lambda = 3.4$, which will be used as primary experimental source for comparison in this study, are given in Table 5. For the experimental and full scale tests, a range of operating conditions were run, from a very light load at 2.2% MCR (Maximum Continuous Rating) to a condition of 73.4% MCR. Two conditions have been used in this computational study, 16.1% MCR and 32.0% MCR, see Table 6.

The studies described below consist of one simulation for the hull and propeller configuration, as well as sim-

[3]SONIC, grant agreement 314394, European Union 7th Framework Programme

ulations for the propeller alone, mounted on an inclined shaft. The appended hull-propeller configuration is made for a single hull but without the free surface and using a symmetry condition along the centre line of the vessel. The hull is however trimmed according to tested conditions. This simplification was a necessary compromise with respect to the computational complexity when simulating a the full hull with cavitating propeller. Further, the rudder was excluded to simplify meshing, which however may have some impact on directionality of radiated noise. For the stand-alone propeller, we did not mimic any existing experimental set-up. Instead, we used a shaft inclination that corresponds to the appended geometry, 8.35° to the inflow, with the shaft extended upstream, and running similar conditions. This was done to test a configuration of intermediate complexity for noise simulations, but still be able to relate to the full simulation. Similar experimental tests have been performed by Aktas et al. (2015), with the same propeller but with systematic variations of shaft inclination, advance coefficient, and cavitation number. We have here not tried to mimic these conditions, since the intention was to have data to compare with the appended configuration. The primary difference is that in Aktas et al. (2015), the propeller was mounted upstream the shaft, while here it is downstream. Some qualitative comparisons are however possible.

The propeller was run both in cavitating conditions and non-cavitating conditions, Condition 2 and Condition 3 respectively in Table 6, while the results presented here for the appended configuration only is for cavitating conditions, Condition 1. Both the cavitating conditions are run with the same environmental pressure and the difference in cavitation number stems from the change in advance velocity and rotational speed. The shaft inclination for the stand-alone propeller case is rather small and does not give a very large tangential velocity component to the propeller, thus the transient behaviour of the loading is weak. Considering the wake fraction in the hull-propeller configuration, running the same condition here gives a propeller that is not as loaded. Ideally, conditions of thrust identity should be used, but it was out of scope for this study to iterate conditions to find equal K_T and thus the higher loading condition from the measurement campaign, Condition 2 of Table 6, was used for these studies. This means that the propeller is run at slightly higher loading as stand-alone compared with the hull-propeller configuration. The average thrust coefficient here is $K_T = 0.204$ compared with $K_T = 0.193$ in the self-propelled case at condition 1; stand-alone propeller running at Condition 1 yields $K_T = 0.176$.

Table 5: Main ship and model scale dimensions of the configuration (length scale factor $\lambda = 3.4$).

Quantity	Notation	Value
Length	L_{PP} [m]	4.84
Beam overall	B [m]	2.07
Draft	T [m]	0.93
Propeller diameter	D_p [m]	0.22
Pitch ratio (at 70%)	P/R_P	0.8475
Expanded area ratio	EAR	1.057

Table 6: Operating conditions for simulations.

Notation	V_M [kn]	n [1/s]	σ_n
Condition 1 (16.1% MCR)	2.61	20.96	2.81
Condition 2 (32.0% MCR)	2.94	26.31	1.78
Condition 3 (32.0% MCR)	2.94	26.31	∞

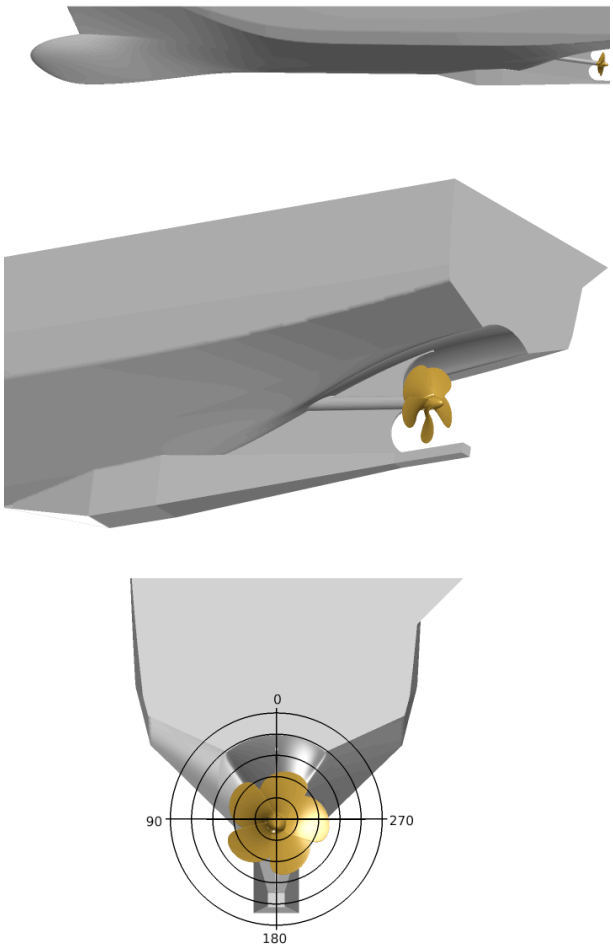

Figure 5: Geometry of the R/V Princess Royal.

Computational configuration

All simulations have been run using a wall-modelled implicit LES approach, as described in the methodology section. First, the simulation for the hull-propeller configuration were run in non-cavitating conditions until a well developed flow was achieved. Then cavitation was initiated, and it was allowed to run for further several propeller revolutions before acoustic sampling was initiated. A similar approach was used for the stand-alone propeller.

For the convective terms, a TVD limited scheme was used, and time stepping was performed with an implicit second order scheme. The time step was set to $1/20$ of a degree of propeller revolution, which, for the hull propeller configuration, results in $\Delta t = 6.5356 \cdot 10^{-6}$, and for the stand-alone propeller simulations, $\Delta t = 5.278939 \cdot 10^{-6}$. This setting leads to a maximum Courant number in the range $Co = 1.5 - 1.8$, where the maximum occurs only in the small cells around the propeller blade tip. To ensure stable simulations, two outer iterations were performed in the OpenFOAM PIMPLE loop. Sampling of variables on the integral surfaces, for the acoustic post-processing, are made every 10^{th} time step, thus corresponding to two samples every degree of propeller rotation. The acoustic sampling was performed for eight propeller revolutions, started after disregarding initial transients, for the stand-alone propeller simulations and 10 revolutions for the propeller-hull configuration.

For the hull-propeller simulation, a larger box domain has been created around one of the two catamaran hulls, with a symmetry plane in the centre of the vessel. The box extends $2L_{PP}$ upstreams, $3L_{PP}$ down stream, and has $2L_{PP}$ to the side and below the hull, see Figure 6. The propeller is enclosed in a large cylinder, with diameter $6D_p$, and the shaft extends $3D_p$ upstreams the propeller and the outlet is located $6D_p$ downstream, see Figure 7. The propeller is enclosed in a smaller cylinder puck that rotates with the propeller. The same coordinate system has been used for both configurations, thus this rotating propeller puck is identical in all cases, as well as the shaft line.

The mesh for the hull was created using Hexpress™, and was provided by MARIN within the SONIC project cooperation. It is thus an oct-tree unstructured hexahedral mesh, snapped to the geometry and with an extruded boundary layer mesh. Several refinement boxes had been applied in the stern region, see Figure 8. Similar mesh around the propeller was used in both simulations configurations. It was created in Pointwise®, using a structured quad mesh on the surface of the blades, extruding a hexahedral boundary layer mesh, and then filling the puck domain with unstructured tetrahedral cells using the anisotropic mesh extrusion feature of Pointwise®, T-Rex. In the hull-propeller simulation, a hole was cut in the existing Hexpress™ mesh to accommodate the propeller puck, filling up the gap with a general unstructured mesh. For the stand-alone propeller, an exterior domain was constructed and meshed within Pointwise®, following the same principle as with the propeller. The cell distribution for the hull-propeller configurations is given in Table 7.

Table 7: Number of cells in the computational grids for the hull-propeller configuration, according to cell-type.

#cells/10^6	Hull	Propeller	Total
Hex	20.5	3.2	23.7
Tet	-	1.8	1.8
Prism	-	0.04	0.04
Poly	1.24	0.06	1.3
Total	21.74	5.1	26.84

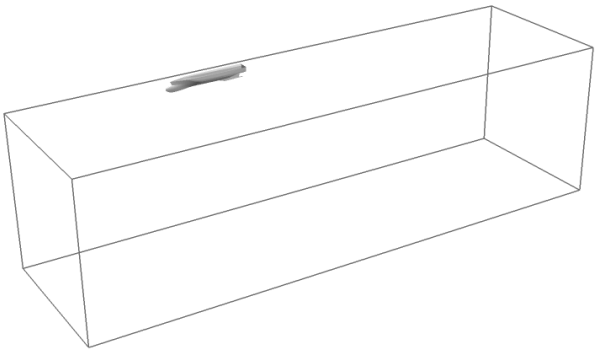

Figure 6: Computational domain for the hull-propeller configuration.

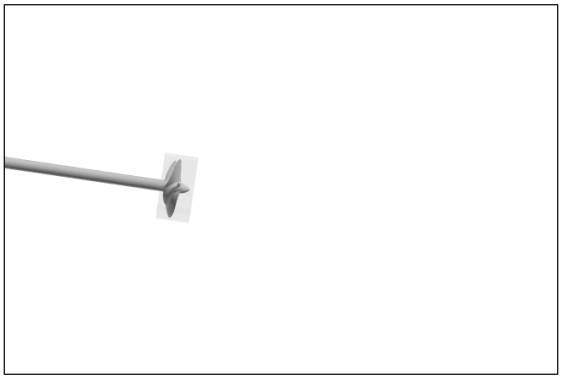

Figure 7: Computational domain for the stand-alone propeller simulations, with the rotating domain shaded.

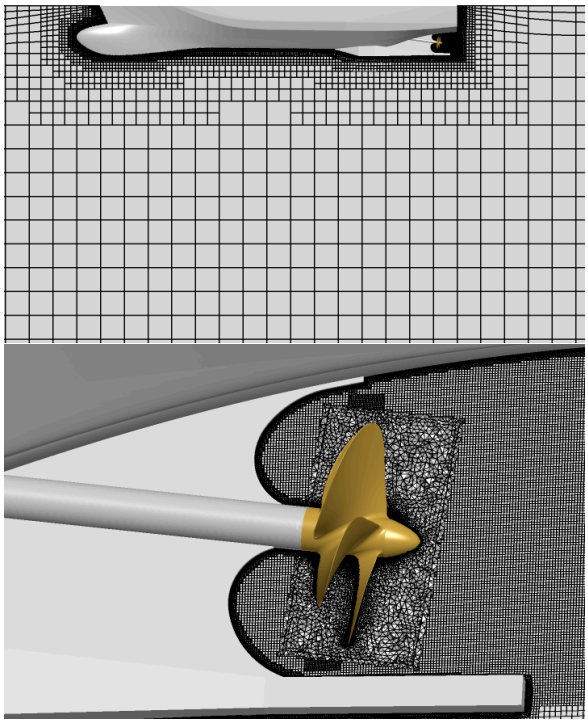

Figure 8: Computational mesh of the hull.

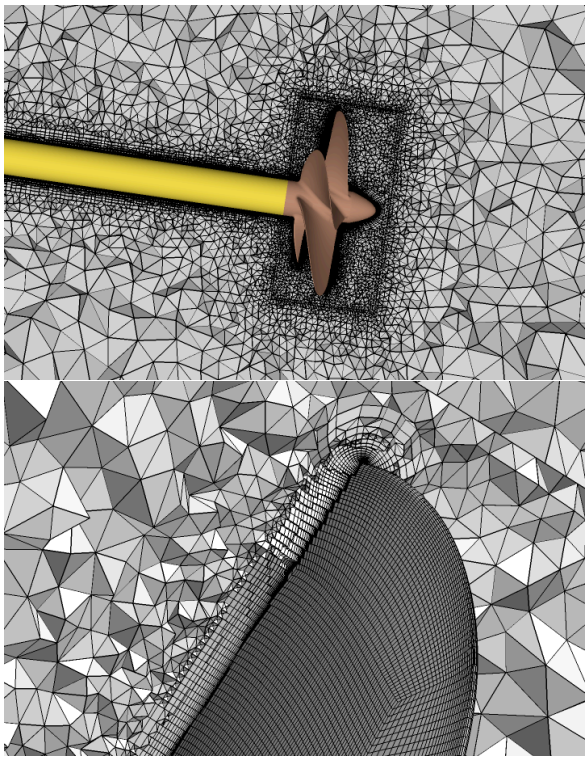

Figure 9: Computational mesh of the propeller. Note that the similar mesh around the propeller was used in both simulation configurations, up to the rotating puck surrounding the propeller.

For the acoustic sampling for the FWH post-processing, a sampling surface was extracted from the hull and domain meshes respectively. A circular cylinder was defined, with a horizontal axis through the centre of the propeller and a radius to fit just outside of the propeller puck but not cutting the hull. The cylinder started just after the skeg, upstream of the propeller, and extended $2D_P$ downstream, where detailed structures in the propeller slip were no longer resolved. Then, the outer faces of the cells cut by this cylinder was used to form the sampling surface, see Figure 10. The sampling surface was left open. During post-processing of the acoustic results, three hydrophones where placed in the same location as in the CNR-INSEAN experiments. There, the hydrophones were place on 1 m distance from the propeller centre, with one straight aft in the propeller slip, H1, one slightly to the outward side, H7, and one slightly down, H8, see Figure 11. Further, a series of hydrophones were placed straight below the propeller, on distances 1 m, 2 m, 5 m, and 10 m.

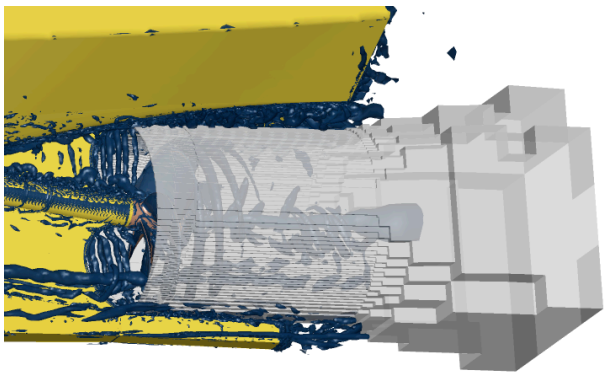

Figure 10: The surface where data for the Ffowcs-Williams Hawkings integrals were sampled is shown in grey.

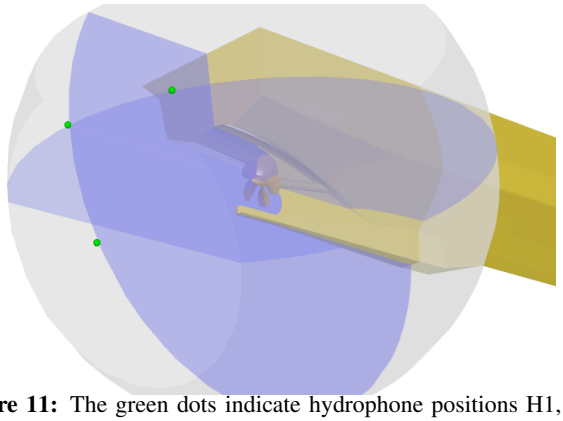

Figure 11: The green dots indicate hydrophone positions H1, H7, and H8, as denoted in the CNR-INSEAN experiments, placed on a sphere at 1 m distance from the propeller centre.

Table 8: Hydrophone location, in relation to propeller cap tip.

Name	Location	Distance
H1	straight behind	1 m
H2	straight below	1 m
H3	straight below	2 m
H4	straight below	5 m
H5	straight below	10 m
H6	behind and inward	1 m
H7	behind and below	1 m
H8	behind and outward	1 m

Stand-alone propeller on inclined shaft

Flow behaviour

An overview of the flow around the stand-alone propeller is given in Figures 13 and 14 for the two tested conditions, with a snapshot of the propeller inflow displayed in Figure 12. For the cavitating case, Condition 2, a distinct sheet cavity is developing along the leading edge of the blade, present on all blades all time. There is no tip vortex cavitation in the simulations; the mesh resolution is clearly too low to capture this demanding phenomenon. We can see the influence of the tangential wake component, induced by the inclined shaft configuration, on cavity extent and the low pressure region in the tip region of the blade. This concerns both the thickness and the radial position of where the sheet cavity starts on the blade, which is much earlier in the top positions and when the blade is moving down than in the bottom ones. The same phenomenon is noted in the wetted simulation, where the surface streamlines indicate a longer vortex build-up in the same blade positions. There are minor differences between the two conditions, only induced by the flow around the predicted sheet cavity.

For a comparison of propeller performance between non-cavitating and cavitating conditions, see Table 9; we here follow the conventional definition,

$$J = \frac{V_A}{nD_P}, K_T = \frac{T}{\rho n^2 D_P^4}, K_Q = \frac{Q}{\rho n^2 D_P^5}, \eta_0 = \frac{J}{2\pi}\frac{K_T}{K_Q}, \quad (6)$$

where the forces are measured along the shaft, and the other parameters are given as Condition 2 (cavitating) and Condition 3 (non-cavitating) in Table 6. The mean values, $m(\cdot)$, and standard deviation, $\sigma(\cdot)$, are based on eight revolutions of steady running conditions at $J = 0.51$. We see a slight increase in the mean torque coefficient, while the mean thrust is more or less constant, when running in cavitating conditions. Considering the variability, we note that cavitation seems to stabilise the flow somewhat as both $\sigma(K_T)$ and $\sigma(K_Q)$ is lower by a factor of around 3 for Condition 2; however the levels are very small. Compared with the experimental results presented in Aktas et al. (2015), we note a general higher K_T in our simulations while K_Q is more similar, thus also the efficiency, η_0, is considerably higher. The reason for this is believed to be related to the difference in configuration, where the upstream inclined shaft arrangement in the simulations will lead to a wake that is not present in the experiments.

Cavitation extent is reasonably predicted, making a qualitative comparison with Figure 6 in Aktas et al. (2015). As commented above, no tip vortex cavitation is predicted but this is expected considering the low mesh resolution in the blade wake. However, looking at the sheet cavity in the top position, the cavity starts at the leading edge at a radius lower than 0.5, and grows to a rather thick sheet towards the top of the blade. Water then penetrates below the cavity and detaches the sheet that is twisted into the tip vortex. Variation in cavity extent can be noticed around the revolution, with larger cavity in top position. Further, there are some dynamics in the cavity behaviour, but not substantial, thus it is expected that the blade passing frequency will dominate the emitted noise from the propeller.

Table 9: Propeller characteristics - stand-alone.

	$m(K_T)$	$\sigma(K_T)$	$m(K_Q)$	$\sigma(K_Q)$
Cond 2	0.2036	$1.21{\cdot}10^{-4}$	0.0287	$1.35{\cdot}10^{-5}$
Cond 3	0.2035	$2.94{\cdot}10^{-4}$	0.0275	$3.1{\cdot}10^{-5}$

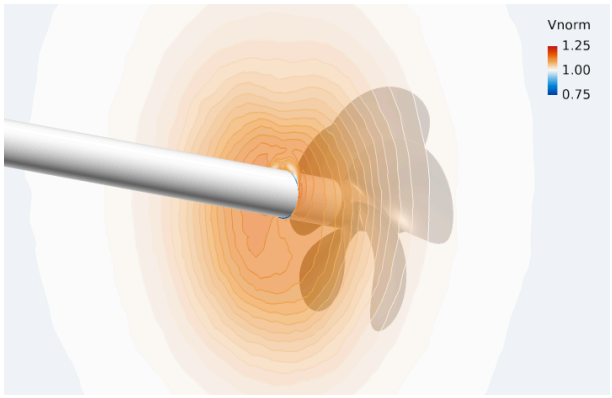

Figure 12: Effective inflow to the propeller on inclined shaft; contours of longitudinal velocity normalised by V_A.

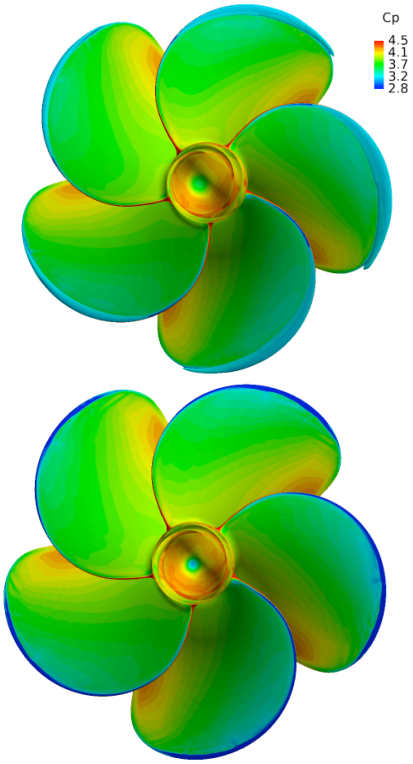

Figure 13: Pressure distribution on the stand-alone propeller for Condition 2 (top) and Condition 3 (bottom); for the former also an iso-surface of vapour is displayed.

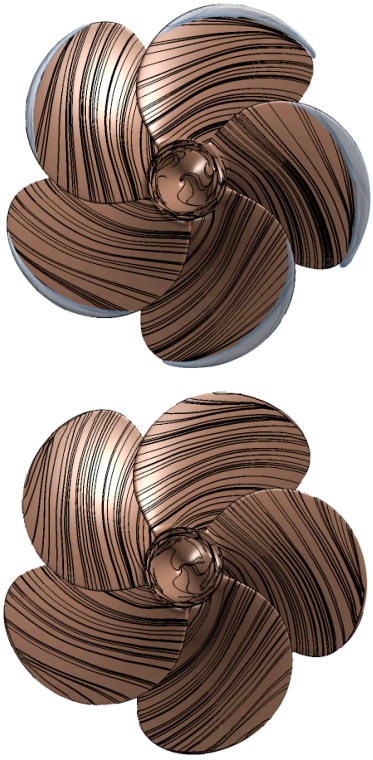

Figure 14: Surface streamlines on the stand-alone propeller for Condition 2 (top) and Condition 3 (bottom); for the former also an iso-surface of vapour is displayed.

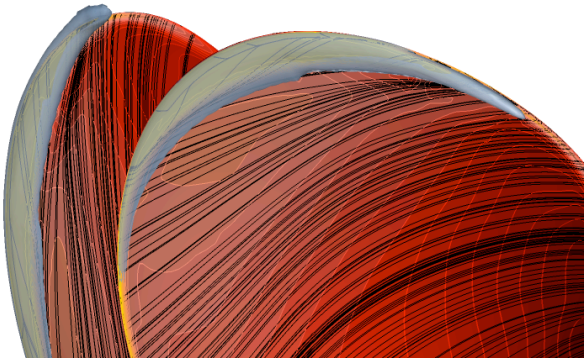

Figure 15: Details of cavitation on the stand-alone propeller for Condition 2.

Acoustic results

The predicted sound pressure level, SPL, for the two conditions is plotted in Figures 16 and 17; here extracted for hydrophone H7, below and to the side, see Table 8, but the directional dependence is expected to be very low in this configuration. A qualitative comparison will be made to the experimental results reported by Aktas et al. (2015), but due to the differences in configuration and conditions no detailed quantitative comparison is included. Focus is instead on comparing numerical noise predictions from the two different conditions.

Overall, the SPL spectra are quite noisy, especially above around 1,100 Hz; this holds for both conditions. The sampling time is short, only eight revolutions, which contributes to the noisiness, but the sampling frequency is almost 19,000 Hz, and thus well above this range. The methodology to extract a sampling surface from cell faces in the mesh, instead of interpolating to a sampling point on a smooth geometrical surface, was developed to avoid noise from interpolation and has been validated on analytical acoustic test functions. The reason for the high level of signal noise thus needs further investigations to clarify.

The general level is the same in both conditions, which is surprising as it was expected that the sheet cavitation would greatly increase the predicted SPL for Condition 2. This lack of cavitation amplified sound was however also noted in (Aktas et al., 2015), where only certain conditions would give distinct differences for different cavitation numbers. The simulations predict a somewhat lower SPL compared with the experiments, where the overall SPL in lower frequencies were just above 90 dB, while we here see levels of just below 90 dB.

The most distinctive tonal for both conditions is the propeller revolution frequency at 26 Hz. The peak is however considerably wider for the cavitating condition, Condition 2, which is expected to be a result of cavitation dynamics. Further, the BPF, blade passing frequency, at 132

Hz is considerably more distinct in the cavitating conditions, while the opposite holds for the 2nd BPF. Some other peaks are visible in the spectra, but are perhaps questionable with respect to the noisy signal.

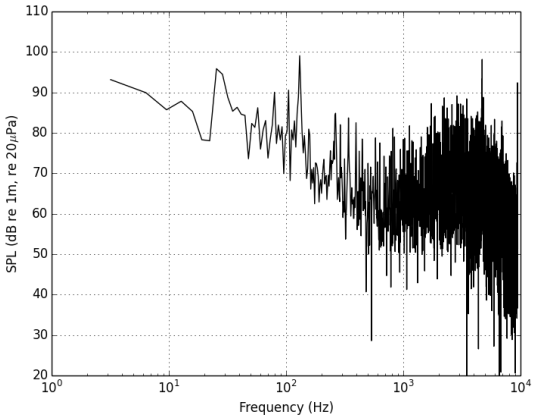

Figure 16: Noise prediction for the stand-alone propeller at Condition 2 (cavitating) at hydrophone H7.

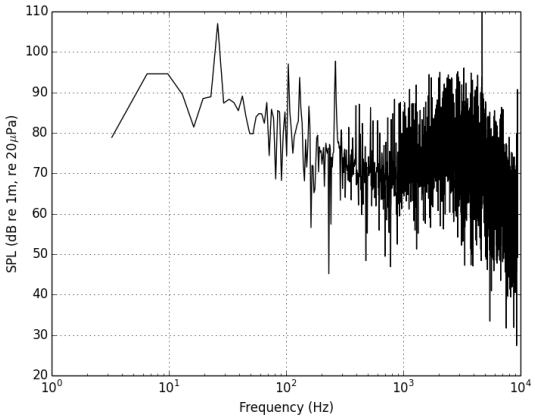

Figure 17: Noise prediction for the stand-alone propeller at Condition 3 (non-cavitating) at hydrophone H7.

Propeller-hull

Flow behaviour

We will here limit the attention to the aft-ship flow, with a focus on structures that are expected to have an impact on noise generation. An overview of the flow is given in Figure 18, visualised by limiting streamlines on the hull, several contour planes of the longitudinal velocity, and a close-up of the flow structures around the propeller. Here, as well as in Figure 20, flow structures are visualised by an iso-surfaces of a structure function, $||\nabla \times \mathbf{v}|| - ||\nabla \mathbf{v}||$, which is very similar to the Q-function but works better when post-processing on this type of grid. The hull has several sharp features that control the flow into the propeller: there is a tunnel to accommodate the propeller with sharp chines, the shaft is supported by a skeg where there are distinct edges in the intersection, and a tapered box structured skeg plate is mounted on the keel and extends aft along the skeg to support the rudder (which itself is not present in this simulation). The hull itself is symmetric (except closer to the waterline) but the propeller rotation induces asymmetry to the flow.

In Figure 19, some of the contour planes are visualised separately, starting from where the keel line rises towards the propeller tunnel to right after the propeller; note that the range is different in the last plane after the propeller. Directly, three vortices are formed: one on each side of the skeg plate where it meets the hull, and one on the bottom corner (induced by the rotational propeller suction). The latter is rather weak, and instantaneous snap-shots reveal that there are in fact several small vortices, not one distinct, that are formed by the overflow on the bottom side of the skeg plate; this vortex system will however not reach the propeller and have little impact on noise and unsteadiness in the propulsion system. The two former ones are rather stable, can be traced to move horizontally aft along the skeg, grow in strength, and will end up in the propeller disc, contributing to the unsteady propeller blade load and total thrust variation. On top of the skeg plate, further aft, a second vortex pair is formed that goes below the propeller, visible in the plane closest to the propeller (upstream). As the tunnel starts, we note an overflow around the chines from the hull into the tunnel forming vortices along the chines. A pair of vortices are also formed in the junction between the skeg and the tunnel. Together with the chine vortices, these form a very complex and dynamic flow field in the tunnel close to the hull. Fortunately, this passes above the propeller and is thus not expected to have any major impact on the propulsor characteristics. Finally, there is another vortex pair formed in the junction on top of the shaft where it connects to the skeg. This is also a very dynamic flow structure, instantaneously it is even difficult to discern it as a vortex system, that feeds straight into the root section of the propeller. Visible in the contour plots is also the low velocity thin wake from the skeg, from the skeg plate up to the hull, entering the propeller disc.

Another visualisation of this flow is shown in Figure 20, where the above mentioned structure function is used both for the instantaneous flow field and the time averaged flow field. This figure gives a very clear impression on the unsteadiness of the vortex systems described above. The vortices that originate from the junction between the hull and the skeg plate, the first ones described above, are relatively stable and easily discernible also in the instantaneous flow. The ones on the top side of the shaft are clearly more dynamic, but shown as well developed vortices in the average flow. The system of vortices formed

in the tunnel, however, is very dynamic and the snap-shot does not reveal any coherent vortex structure, while the separate vortices are clear in the averaged flow.

The most interesting difference between the instantaneous and average flow is however the vertical von Kármán vortex shedding from the skeg that is present in the flow, but naturally can not be represented in the averaged flow field; this is quite distinct in Figure 20. The vortex street is further displayed in Figure 21, where horisontal planes of contours of vertical vorticity is shown. The alternating vortices are regularly shed from the skeg and transported right into the propeller. The frequency of this shedding is assessed by analysing velocity and pressure probes in the flow field upstream of the propeller. Although the signal is dominated by the blade passing frequency at 104.8 Hz, the probes were obviously placed too close to the propeller, the shedding frequency seems to be visible at around 35 Hz. This corresponds to a Strouhal number in the range of $St = \frac{fL}{V} \approx 0.1 - 0.3$, which is in the expected range for a rectangular trailing edge.

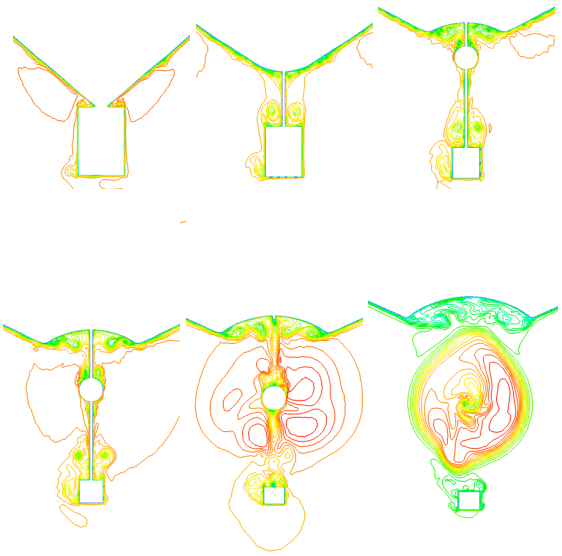

Figure 19: Contour plots of longitudinal velocity from the beginning of the tunnel to just aft of propeller. Note the the range of contours is changed in the last frame to show details in the propeller slip.

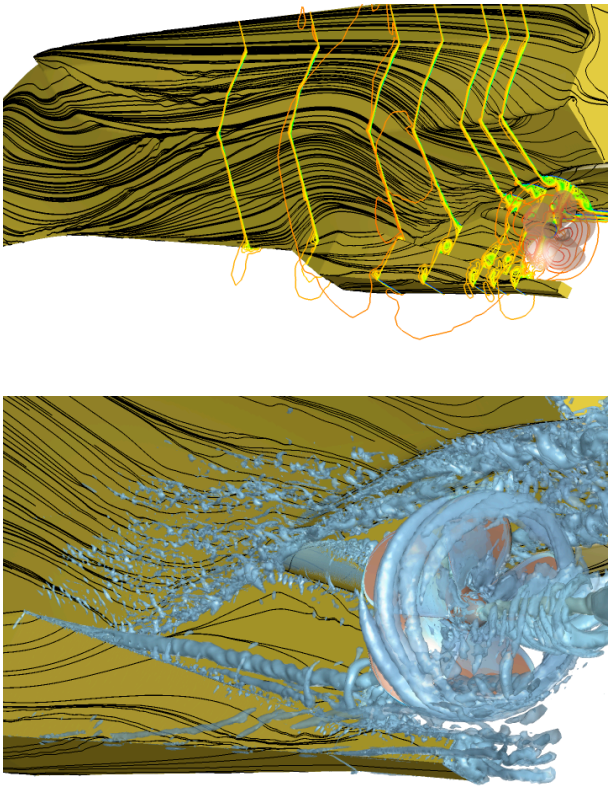

Figure 18: Overview of the predicted flow in terms of limiting streamlines and contour planes of longitudinal veolcity (top) and a flow structure visualisation through an iso-surface of $||\nabla \times \mathbf{v}|| - ||\nabla \mathbf{v}||$ (bottom).

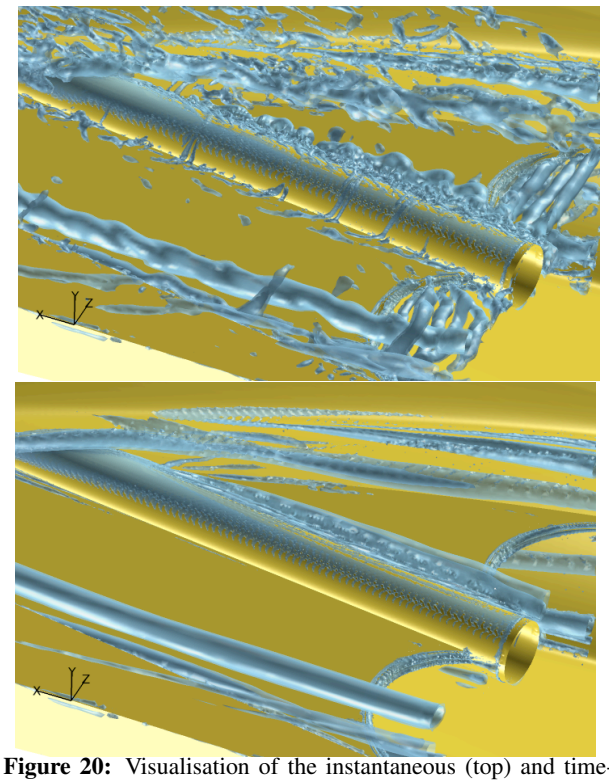

Figure 20: Visualisation of the instantaneous (top) and time-averaged (bottom) flow in the stern; iso-surface of $||\nabla \times \mathbf{v}|| - ||\nabla \mathbf{v}||$.

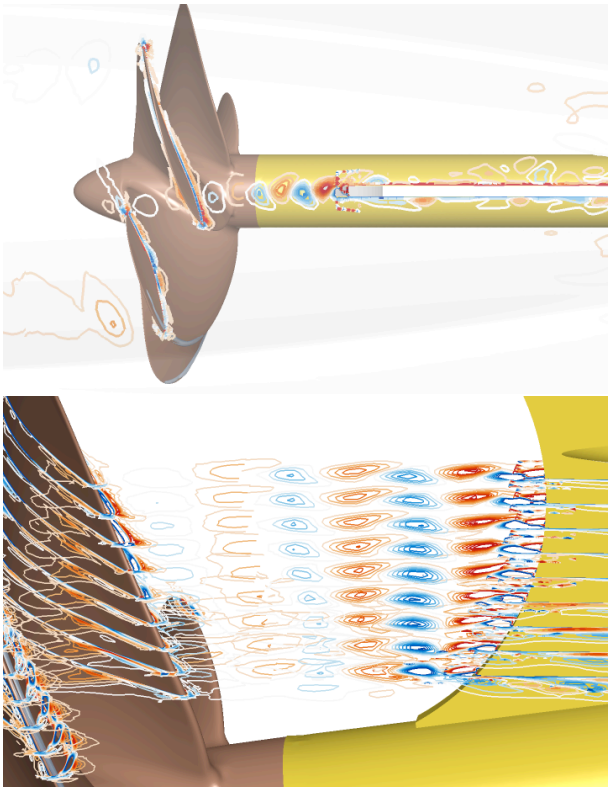

Figure 21: Contour planes of vertical vorticity, indicating the von Kármán vortex shedding from the skeg.

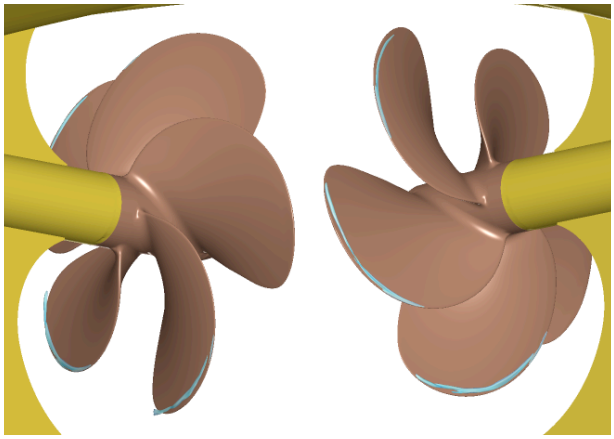

Figure 22: Visualisation of cavitation for the propeller behind hull, Condition 1.

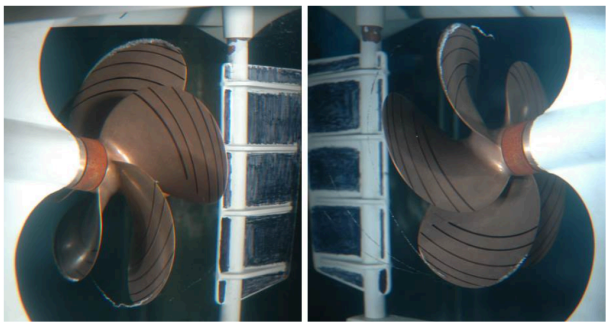

Figure 23: Snapshots from the cavitation experiments performed at Rolls-Royce Hydrodynamic Research Centre (SONIC, 2015a).

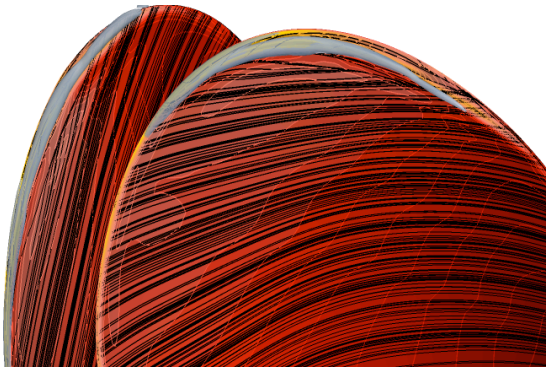

Figure 24: Details of the cavitation on the propeller in behind Condition 1.

Regarding cavitation prediction, the vapour volume is somewhat underpredicted, not only with respect to the lack of tip vortex cavitation but also for the on-blade sheet cavity. Figures 22 and 23 show predicted cavitation from this simulation and experiments performed in the cavitation tunnel at the Rolls-Royce Hydrodynamic Research Centre. We remark that a fair quantitative comparison is difficult, as we can only compare snap-shots of certain times in a highly unsteady flow. The impression is however, that the numerically predicted sheet cavities cover about the same extent of the leading edge, but the sheet grows thicker in the experiments. The dynamic behaviour of the sheet seems to be reasonably predicted, with respect to detachment from the blade surface and the occasional disintegration of a cavity, visible both in the experiments and in the simulation. A detailed view of the flow around the cavity in the top blade position is seen in Figure 24, to be compared with the stand-alone propeller configuration in Figure 15.

Acoustic results

The predicted SPL at hydrophone H7, is plotted in Figure 25 together with experimental results provided by CNR-INSEAN collected in the same position. Also here, we see the same issue with the predicted SPL with respect to

noisy signal as was discussed above for the stand-alone propeller simulations, with results above around 1,100 Hz questionable. The overall trend, including some variation, seems however to follow the experiments to somewhat higher frequencies. The sampling frequency in the simulation was for this case around 15,000 Hz, as it was related to the propeller revolution rate, and sampling time corresponds to 10 propeller revolutions.

In the lower frequency range, up to around 400 Hz, the numerical prediction is greatly underpredicted; there is a clear gap of around 20 dB between simulation and experiments. The cause for this discrepancy is currently not clear to us, and will be further discussed below. In the range of 400 Hz - 1,100 Hz, however, the numerical results agree well with measurements.

There are no distinct peaks at lower frequencies, which is expected due to the relatively short sampling time. The 1st BPF, blade passing frequency, and the 2nd BPF are clearly visible, although at the overall lower level, as noted above. The 2nd BPF peak is predicted to be wider than the 1st BPF, which is inline with the measurements. The experiments indicate a distinct peak at around the 4th BPF, which is not noted in the simulations, although this is a frequency range where we note a large increase in predicted SPL which might shadow this tonal. In the medium frequency range, 400-1,100 Hz, four wide peaks are predicted both in the simulation and the experiment, although the mid-frequencies of those differ sligthly.

The directivity has also been investigated, by comparing the predicted SPL from hydrophones H7 and H8. In the measurements, a clear directivity was detected. This has not been seen in the simulations, where the spectra from H7 and H8 are more or less identical; thus not included separately in this paper. As a basic soundness test of the methodology, Figure 27 shows how the predicted SPL decays with increasing distance between propeller and hydrophone. Further analysis is however required to quantitatively determine the decay rate.

From a methodological perspective, the performance of a Ffowcs-Williams and Hawkings approach with sampling surfaces in the flow field is in an experimental phase. The choice of sampling surface was here made for practical reasons, to fit in the flow domain around the propeller in the constrained aft-ship region. The acoustic integrals were also evaluated on the hull surface. The comparison in predicted SPL from these two alternatives are shown in Figure 26. In the higher frequency range, from about 600 Hz, the spectra overlap, but below that some peaks are missing when not using the sampling surface. In the low frequency range, below 100 Hz, the radiated noise evaluated using the hull surface is about 10 dB lower compared when using the sampling surface.

The analysis shows both promises and disappointments. Several of the features in the measured spectrum are captured in the simulation, but the discrepancy in the low frequency range needs to be understood, as well as the lack of directivity. Even more so as the predicted SPL then agrees well in the medium frequency range. Some possible explanations have been discussed, where the first naturally is the lack of predicted tip vortex cavitation. This is expected to contribute significantly to underwater radiated noise, but perhaps rather in the broad band range of the spectrum. However, the attached sheet is also underpredicted. The impact of this is difficult to assess considering the lack of difference between conditions in the stand-alone propeller simulation, also reported in the literature from experiments.

The missing cavitating tip vortex system can also be expected to be responsible for the lack of directivity of the radiated noise in the simulations, as the noise sources in the present results are enclosed in a rather small region close to the propeller and not extending far aft as in the experiments. The exclusion of the rudder in the simulations may also contribute to the discrepancy.

One further important difference between numerical simulations and experiments, is related to the free surface, which is not represented in the numerical simulations. Further, the top boundary could not be placed in a position representative of the still water surface but was placed much further from the propeller. Acoustic reflection at this boundary is thus not correctly represented in the numerical simulation compared with the experiments that were performed with free surface in the CNR-INSEAN large circulating water channel.

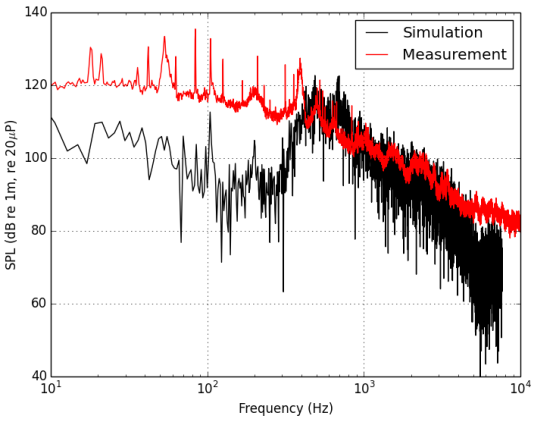

Figure 25: Noise prediction at hydrophone H7 in comparison with experiments from CNR-INSEAN.

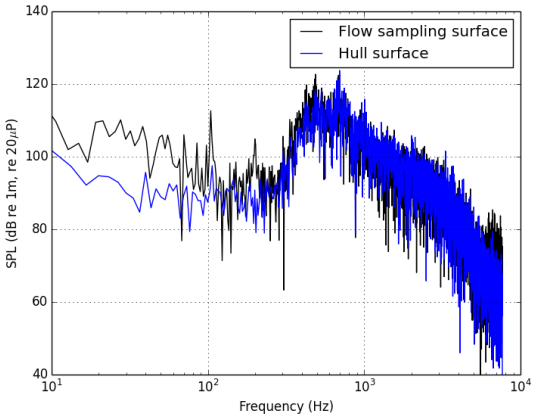

Figure 26: Predicted SPL at hydrophone H7 when using the sampling surface in the flow domain compared with the hull surface.

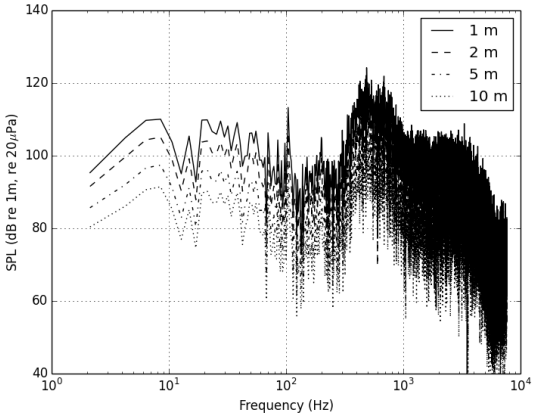

Figure 27: Noise prediction at varying distances below the propeller.

CONCLUSIONS

The work presented in this paper is an exploration study of the feasibility to predict underwater radiated noise from a ship propeller, using resolved flow simulations and an acoustic analogy. The basic methodology is well established to predict aeroacoustic noise at medium to high Ma number. Interest and applications related to low Ma hydroacoustic conditions, especially considering cavitation, have just started to emerge. Both theoretical and practical issues are abundant and need further studies before methodologies for detailed shipping noise prediction through numerical simulations can be used as a well established and reliable tool.

The flow in the aft of a ship is highly transient and flow dynamics is expected to influence radiated noise, both in terms of general noise levels and with respect to peaks in the spectrum. To have a reasonable prediction of radiated noise, it seems clear a flow resolving simulation methodology is needed, like LES or hybrid RANS/LES. An unsteady RANS can only be expected to capture the lower harmonics of the blade passing frequency, often then more of interest in terms of ship vibrations and pressure pulses on the hull plating than with respect to underwater radiated noise. The results presented here show flow features influencing the propulsion system that can not be represented with a RANS approach.

Cavitation volume and the dynamics of cavitation are, for the same reasons as just mentioned, vital to capture. In the simulation results in this work, the sheet cavity volume was underpredicted while the dynamics seemed qualitatively correct. Simulation of cavitating flows is still challenging, although the maturity has increased in the past five years. High resolution is required also for the sheet cavitation, both on the blade surface and off the blade. Here, around 5 M cells were used in the propeller puck, which might not be sufficient. The unstructured approach, however, makes clustering of cells in interesting regions possible yielding an efficient use of the computational effort. Future work will need to include further studies on how increased mesh resolution influences sheet cavity prediction on a propeller in behind condition and the associated radiated noise.

The cavitating tip vortex as a noise source forms an extreme challenge for CFD based noise prediction. With the expected resolution requirement to be able to sustain the low pressure in a vortex core to keep it cavitating, several hundreds of millions of cells would be needed. A separate treatment of the vortex noise thus seems necessary.

With respect to the noise prediction methodology for low Ma flows, and the implementation we have done in OpenFOAM, we found a good prediction for the circular cylinder while the cavitating cases showed discrepancies, but are also more difficult to analyse and evaluate. We could not within the scope of this study determined whether this is related to how sampling surface was defined, its shape and location; issues with how the acoustic analogy handles cavitation noise sources; or with the flow prediction itself, then related to the under predicted vapour volume and lack of cavitating tip vortex.

In view of this, we find that we lack basic validation data for radiated noise from cavitating flows, that are easy to replicate with the suggested simulation methodology. This is also clear from previously the published studies exploring similar methodology (Lidtke et al., 2015, 2016) The stand-alone propeller as investigated at Newcastle University (Aktas et al., 2015) is a case that could be interesting to study further. However, the issue with the impact of the cavitating tip vortex needs to be handled. Further, the experiments only document clear increased noise lev-

els due to cavitation for certain conditions. To clearly be able to develop and evaluate the methodology as a predictive simulation tool, a well documented dataset in a simple flow configuration and with distinct impact from sheet cavitation would be much useful.

ACKNOWLEDGEMENTS

The authors wish to thank other partners of the SONIC project involved in the investigation of the configuration under study, for fruitful scientific discussions. Especially MARIN and Pierre Crepier who shared their computational meshes, and Dr. Mario Felli at CNR-INSEAN who provided experimental data for the hull-propeller configuration.

The simulations were performed on resources at C3SE, Chalmers Centre for Computational Science and Engineering, and NSC, National Supercomputer Centre in Sweden, provided by the Swedish National Infrastructure for Computing (SNIC).

This paper was partially supported with funding from the European Union 7th Framework Programme under project SONIC (grant agreement number 314394). Support for this work has been provided by Rolls-Royce Marine through the University Technology Centre in Computational Hydrodynamics hosted at the Deptartment of Shipping and Marine Technology at Chalmers.

REFERENCES

Aktas, B., Atlar, M., Turkmen, S., Korkut, E., and Fitzsimmons, P., "Systematic cavitation tunnel tests of a Propeller in uniform and inclined flow conditions as part of a round robin test campaign," Ocean Eng., 2015.

Aktas, B., Atlar, M., Turkmen, S., Shi, W., Sampson, R., Korkut, E., and Fitzsimmons, P., "Propeller cavitation noise investigations of a research vessel using medium size cavitation tunnel tests and full-scale trials," Ocean Eng., 2016.

Asnaghi, A., "Developing Computational Methods for Detailed Assessment of Cavitation on Marine Propellers," Licentiate report, Chalmers University of Technology, 2015.

Atlar, M., Aktas, B., Sampson, R., Seo, K.-C., Viola, I.-M., Fitzsimmons, P., and Fetherstonhaug, C., "A multi-purpose marine science and technology research vessel for full-scale observations and measurements," 3rd International Conference on Advanced Model Measurement Technologies for the Marine Industry, 2013.

Barton, I. E., "Comparison of SIMPLE- and PISO-type Algorithms for Transient Flows," Int. J. Num. Meth. Fluids, 26, 1998.

Bensow, R. E., "Simulation of Unsteady Propeller Blade Loads Using OpenFOAM," 16^{th} Numerical Towing Tank Symposium, NuTTS'13, Mülheim, Germany, sep 2013.

Bensow, R. E., "Large Eddy Simulation of a Cavitating Propeller Operating in Behind Conditions with and without Pre-Swirl Stators," 4th International Symposium on Marine Propulsors, smp'15, 2015.

Bensow, R. E. and Bark, G., "Implicit LES Prediction of the Cavitating Flow on a Propeller," J. Fluids Eng., 2010.

Bensow, R. E. and Fureby, C., "On the Justification and Extension of Mixed Methods in LES," J. Turbulence, 8, 2007.

Bensow, R. E. and Liefvendahl, M., "Implicit and Explicit Subgrid Modeling in LES Applied to a Marine Propeller," 38th Fluid Dynamics Conference and Exhibit, volume AIAA-2008-4144, Seattle, WA, USA, 2008.

Blake, W. K., "Mechanics of flow-induced sound and vibration," Academic Press, 1986.

Cantwell, B. and Coles, D., "An experimental study of entrainment and transport in the turbulent near wake of a circular cylinder," J. Fluid Mech., 136:321–374, 1983.

Cox, J. S., Brentner, K. S., and Rumsey, C. L., "Computation of vortex shedding and radiated sound for a circular cylinder: Subcritical to transcritical Reynolds numbers," Theoretical and Computational Fluid Dynamics, 12:233–253, 1998.

Curle, N., "The Influence of Solid Boundaries upon Aerodynamic Sound," Proc. R. Soc. Lond. A, 231:505–514, 1955.

Etkin, B., Korbacher, G. K., and Keefe, R. T., "Acoustic radiation from a stationary cylinder in a fluid stream (aeolian tones)," The Journal of the Acoustical Society of America, 29:30–36, 1957.

Farrell, P. E. and Maddison, J. R., "Conservative interpolation between volume meshes by local Galerkin projection," Comput. Methods Appl. Mech Engrg, 200(89), 2011.

Felli, M., Falchi, M., and Dubbioso, G., "Experimental approaches for the diagnostics of hydroacoustic problems in naval propulsion," Ocean Engineering, 106:1–19, 2015 ISSN 0029-8018 doi: http://dx.doi.org/10.1016/j.oceaneng.2015.06.049.

Ffowcs-Williams, J. E. and Hawkings, D. L., "Sound Generation by Turbulence and Surfaces in Arbitrary Motion," Proc. R. Soc. Lond. A, 264(1151):321–342, 1969.

Francescantonio, P. D., "A new boundary integral formulation for the prediction of sound radiation," Journal of Sound and Vibration, 202(4):491–509, 1997.

Franke, J. and Frank, W., "Large-eddy simulation of the flow past a circular cylider at Re_D=3 900," Journal of Wind Engineering and Industrial Aerodynamics, 90: 1191–1206, 2002.

Fureby, C., "Large Eddy Simulation of Ship Hydrodynamics," 27th Symposium on Naval Hydrodynamics, Seoul, Korea, 2008.

Grinstein, F. F., W., L. M., and Rider, editors "Implicit Large Eddy Simulation: Computing Turbulent Fluid Dynamics," Cambridge University Press, Cambridge, England, 2007.

LaTorre-Iglesias, E., Thompson, D. J., and Smith, M. G., "Experimental studdy of the aerodynamic noise radiated by cylinders with different cross-sections and yaw angles," Journal of Sound and Vibration, 361:108–129, 2016.

Li, D.-Q., Hallander, J., Johansson, T., and Karlsson, R., "Cavitation dynamics and underwater radiated noise signature of a ship with a cavitating propeller," Salvatore, F., Broglia, R., and Muscari, R., editors, VI International Conference on Computational Methods in Marine Engineering, Rome, Italy, 2015.

Lidtke, A. K., Humphrey, V. F., and Turnock, S. R., "Feasibility study into a computational approach for marine propeller noise and cavitation modelling," Ocean Engineering, 2015 ISSN 0029-8018 doi: http://dx.doi.org/10.1016/j.oceaneng.2015.11.019.

Lidtke, A. K., Turnock, S. R., and Humphrey, V. F., "Characterisation of sheet cavity noise of a hydrofoil using the Ffowcs Williams–Hawkings acoustic analogy," Computers & Fluids, 130:8–23, 2016 ISSN 0045-7930 doi: http://dx.doi.org/10.1016/j.compfluid.2016.02.014.

Liefvendahl, M. and Bensow, R. E., "Simulation-Based Analysis of Hull-Propeller Interaction for a Single-Screw Transport Ship," 30th Symposium on Naval Hydrodynamics, 2014.

Parnaudeau, P., Carlier, J., Heitz, D., and Lamballais, E., "Experimental and numerical studies of the flow over a circular cylinder at Reynolds number 3 900," Physics of Fluids, 20(085101), 2008.

Patankar, S. V. and Spalding, D. B., "A calculation procedure for heat, mass and momentum transfer in three-dimensional parabolic flows," Int. J. Heat Mass Transfer, 15, 1972.

Pérot, F., Auger, J.-M., Giardi, H., Gloerfelt, X., and Bailly, C., "Numerical prediction of the noise radiated by a cylinder," 9th IAAA/CEAS Aeroacoustics Conference and Exhibit, number AIAA-2003-3240, Hilton Head, SC, USA, 2003.

Phillips, O. M., "The intensity of Aeolian tones," Journal of Fluid Mechanics, 1(6):607–624, 1956.

Piomelli, U., "Wall-layer models for large-eddy simulations," Progress in Aerospace Sciences, 44:437–446, 2008.

Sagaut, P., "Large eddy simulation for incompressible flows.," Springer-Verlag, 2002.

Sauer, J., "Instationär kavitierende Strömungen - Ein neues Modell, basierend auf Front Capturing (VoF) und Blasendynamik," PhD thesis, PhD thesis, Karlsruhe University, 2000.

SONIC, "D1.3 – Validation Studies," Technical report, SONIC Project, EU FP7, no 314394, 2015a.

SONIC, "D2.5 – Full Scale Radiated Noise Measurements," Technical report, SONIC Project, EU FP7, no 314394, 2015b.

Spalding, D. B., "A Single Formula for the "Law of the Wall"," Journal of Applied Mechanics, pages 455–458, 1961.

Turunen, T., "Analysis of Multi-Propeller Marine Applications by Means of Computational Fluid Dynamics," Master's thesis, Aalto University, 2014.

Weller, H. G., Tabor, G., Jasak, H., and Fureby, C., "A tensorial approach to computational continuum mechanics using object-oriented techniques," Computers in Physics, 12(9):620–631, 1998.